

Laver-derived Carbon as an Anode for SIBs with Excellent Electrochemical Performance

Yingjie Zhang¹, Hongyu Cheng¹, Jiaming Liu³, Xue Li^{1,*}, Ziyi Zhu^{1,2,*}

¹ National and Local Joint Engineering Laboratory for Lithium-ion Batteries and Materials Preparation Technology, Faculty of Materials Science and Engineering, Faculty of Metallurgical and Energy Engineering, Kunming University of Science and Technology, Kunming 650093, PR China

² School of Environment and Energy, South China University of Technology, Guangzhou 510006, PR China

³ Faculty of Materials Metallurgy and Chemistry, Jiangxi University of Science and Technology, Ganzhou 341000, PR China

*E-mail: 438616074@qq.com, 471096347@qq.com

Received: 1 March 2020 / Accepted: 14 April 2020 / Published: 10 May 2020

In this work, laver-derived sheet-like carbon materials (SCMs) with wrinkles were prepared via a simple pyrolysis method at high-temperature. The electrode material has an open morphology and structure, and exhibits excellent electrochemical performance. The SEMs results show that the carbon material exhibits a sheet-like structure, and the surface is rich in groove structures. As determined by BET analysis, the specific surface area (SSA) reaches 24 m²/g, and the average pore diameter is 5.187 nm. When tested as an anode in sodium-ion batteries (SIBs), the material exhibits a first discharge capacity of 482.8 mAh/g. It also manifests excellent cycle stability. After 100 cycles at a current density of 20 mA/g, the reversible capacity is 261.1 mAh/g, and the capacity retention rate reaches 99.61%. In addition, it has a good-high rate performance, and can achieve a discharge capacity of 199.1 mAh/g at 100 mA/g.

Keywords: pyrolysis at high temperature, biomass-derived carbon, negative electrode, sodium-ion batteries

1. INTRODUCTION

In view of the high energy utilization rate of sodium-ion storage cells, the abundant sodium resources and their low prices, SIBs have received extensive attention and research [1-5]. However, the size of lithium ions is much smaller than that of sodium ions [6], which will make it difficult for commercial graphite materials to perform the electrochemical process of sodium ion insertion-desorption, so their sodium storage capacity and rate performance are severely limited [7]. Among

many carbon-based materials, hard carbon materials (HCMs) prepared from biomass precursors have a great potential to enhance the properties of sodium-based energy storage materials and are easy to recover and reuse [8].

In recent years, many types of biomass have been reported for the preparation of HCMs such as cherry petals [9], bean dregs [10], dandelions [11], wheat stalks [12], pistachio husks [13], rice husks [14], peanut husks [15] and corncobs [16]. These feedstocks are rich in natural polymers and can be produced and consumed in large quantities. Biomass-derived HCMs usually exhibit an outstanding electrochemical reversible capacity with a good rate performance during the sodium storage process due to their open morphology and structure with enlarged interlayer spacings [17]. From an economic and ecological perspective, it is ideal to use resource-rich biomass materials as precursor materials, which can produce high-performance HCMs [18].

In this work, our research group successfully prepared a SIBs anode material from laver, with excellent electrochemical properties. Laver is a kind of edible algae that has been artificially grown in large amounts. It has a typical algae cell structure and composition, which is conducive to hierarchical porous construction. In addition, laver is rich in polysaccharides and proteins. These special properties will allow biomass-derived HCMs to have lower production costs, smaller volume changes, and higher electronic conductivity, and thus have a superior cycle life and rate performance.

2. EXPERIMENT

2.1 Preparation of materials

The purchased dehydrated laver was washed with ultrapure water or ethanol, and it is dried at 80°C for 12 hours. Then the dried laver was placed in a tube furnace and reacted at 1100°C in a protective atmosphere for 3 hours. After calcination at a high temperature, the laver-derived carbon was treated in a 5 M HCl solution for 30 minutes. Finally, the product was washed with ultrapure ethanol or water, and dried to obtain the laver-derived carbon material.

2.2 Material characterization

XRD is applied to characterize the material composition and crystal structure of the laver-derived carbon materials. The X-ray diffractometer uses a copper target with a $K\alpha$ radiation source, $\lambda = 1.54505$, Ni filter, tube current of 40 mA, and tube voltage of 40 kV. The stepping scanning method is adopted, the scanning speed is 2°/min, and 2θ ranges from 10° to 80°. Raman spectroscopy is commonly applied to observe the proportion of graphitization in HCMs. The applicable laser wavelength is 532 nm, and the wavenumber range is 800-2000 cm^{-1} . SEM is used to characterize the surface morphology of the material, and its operating voltage is 20 kV. SSA and porosity analysis are used to characterize the surface area and porosity of laver-derived HCMs. The degassing temperature is 200°C and degassing is performed for 12 hours. XPS is used to characterize the surface elements of the material and their distribution and types of bonding. The $K\alpha$ monochromatic X-ray source is an

aluminium target with a binding energy of 1486.6 eV.

2.3 Electrochemical measurements

The SCMs, conductive carbon black and carboxymethylcellulose (CMC) are coated into pole pieces at a ratio of 8:1:1, and assembled into a CR2016 button cell for testing. After standing for 6 hours, the battery test system (LAND CT 2001A) is used to perform constant current charge-discharge tests such as low current cycling and rate cycling. The test voltage ranges are 0.01 to 3 V. The AC impedance test uses the electrochemical workstation (CHI660E), in which the frequency range is 10^5 - 10^2 Hz and an amplitude of the AC excitation signal is 1 mV.

3. RESULTS AND DISCUSSION

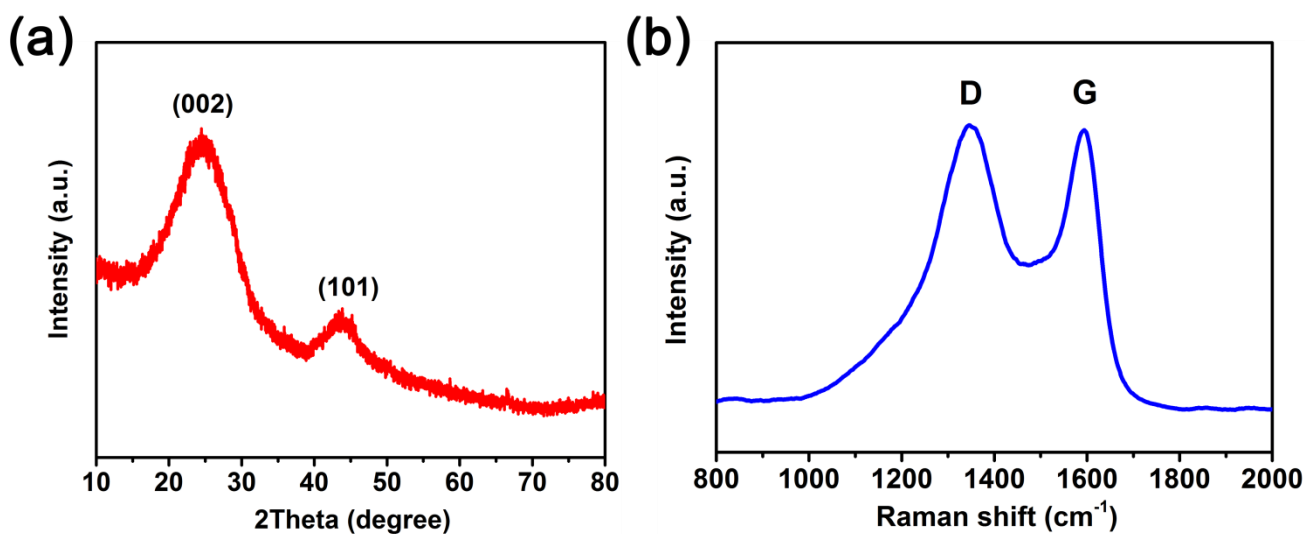


Figure 1. (a) XRD pattern and (b) Raman spectrum of the SCMs

The crystal material structure of the SCMs was analysed by XRD. As displayed in Figure 1 (a), the SCMs has two weak broad diffraction peaks in the XRD pattern, which are located at approximately 24° and 44° , conforming to the (002) and (101) diffraction surfaces of the SCMs, respectively. This result indicates that the SCMs is an amorphous carbon material with a high degree of disorder. At the same time, according to the full width at half maximum of the two diffraction peaks, the thickness of the graphite microchip layer along the c-axis direction is calculated by the Debye-Scherrer formula ($D = k\lambda/\beta\cos\theta$) to be 0.58 nm [19], indicating that the SCMs consists of disordered graphite microcrystals and a small number of stacked graphite microchips.

Raman spectroscopy can also be used to characterize the material microstructure of the SCMs. As displayed in Figure 1 (b), the D band at 1344 cm^{-1} is a defect-inducing band, and the G band at 1595 cm^{-1} is a crystalline graphite band. The peak intensity ratio (I_D/I_G) of the D-band to the G-band

in the Raman spectrum is calculated as 1.015 [20], which confirms that the SCMs is an amorphous carbon material with a highly disordered structure. In addition, using the formula $L\alpha = 44 \times (ID/IG)^{-1}$, the crystallite width ($L\alpha$) along the a-axis direction is calculated as 3.86 nm [21], and the smaller crystallites are beneficial to shorten the transmission distance in the sodium-ion electrochemical reaction and improve the ionic conductivity.

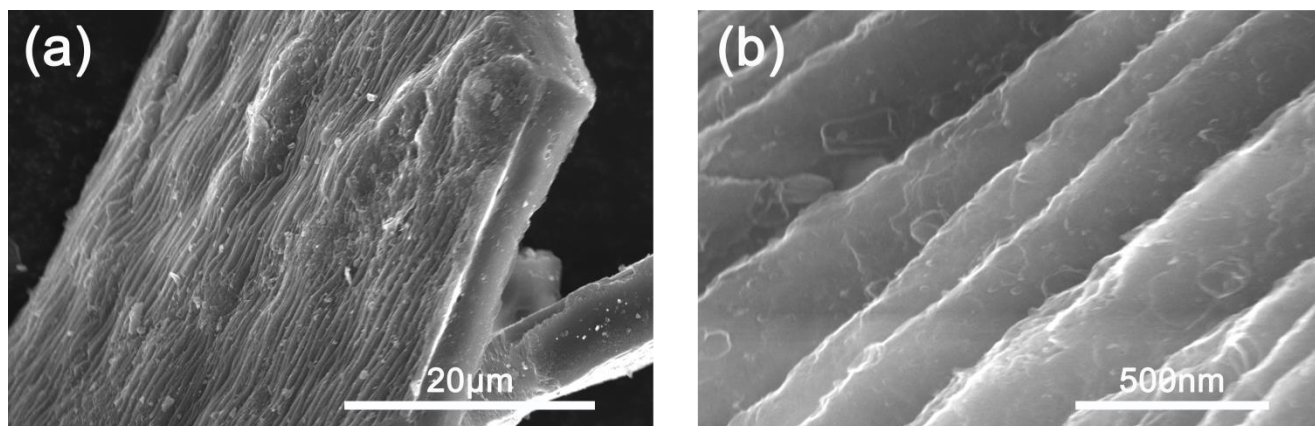


Figure 2. SEM images of the SCMs (a) 250 kx, (b) 8 kx

As shown in Figure 2 (a), the surface of the SCMs has a sheet-like structure with grooves similar to those of the precursor. Observed at 8 k magnification, it can be found that there are linear groove stripes on the front and back surfaces of the laver-derived carbon. When seen with 250 k magnification, it can be observed that the depth of the linear groove is approximately 300 nm. The special topography trough is related to the aquatic surface structure of laver, which can increase the surface area of laver leaves to absorb gas molecules in the water. Therefore, the presence of grooves is beneficial not only to enhance the surface area of laver-derived carbon but increase the number of active sites for electrochemical reactions. Combined with the XRD and SEM images, it can be seen that the processed the SCMs has been transformed into a hard carbon material that retains its original appearance.

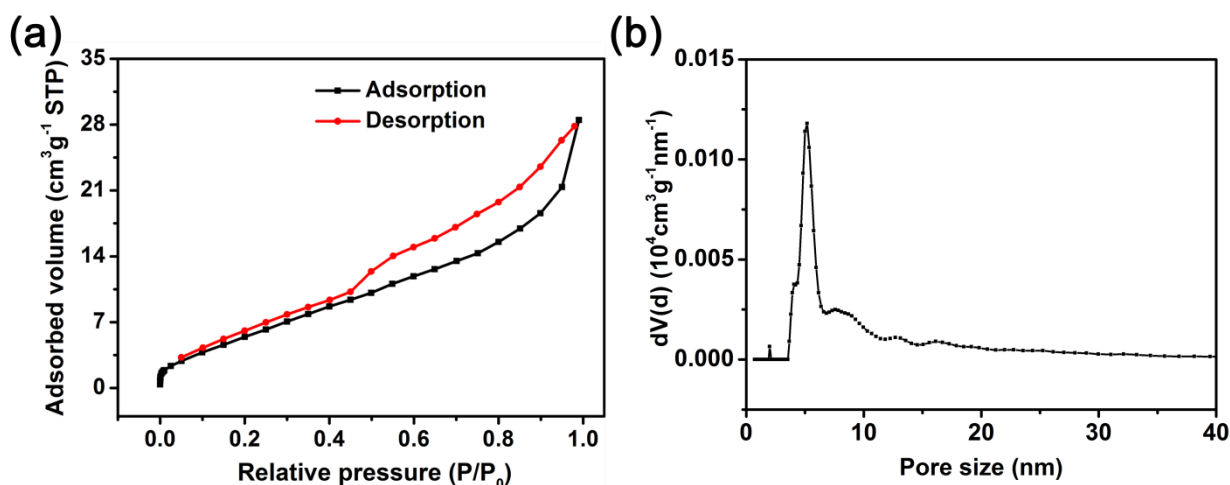


Figure 3. (a) Nitrogen adsorption-desorption isotherms and (b) pore size distributions of the SCMs.

The adsorption-desorption isotherm of N₂ for the SCMs, as shown in Figure 3 (a), is a typical type IV isotherm [22]. It can be inferred that the SCMs has many nano-scale mesopores, which are formed by generating gas during high-temperature processing. At the same time, the hysteresis loop is an H3 type loop when the relative pressure (P/P_0) is 0.45-1.0, showing that the groove structure on the surface of the SCMs is prone to generate slit holes. The results correspond to the SEM characterization findings. As shown in Figure 3 (b), the BJH model is used to calculate the pore size distribution of the SCMs. The average surface pore diameter of the material is 5.187 nm. The BET analysis results show that the SSA of the material is 24 m²/g. These nanoscale mesopores will help store sodium ions in carbon material electrodes.

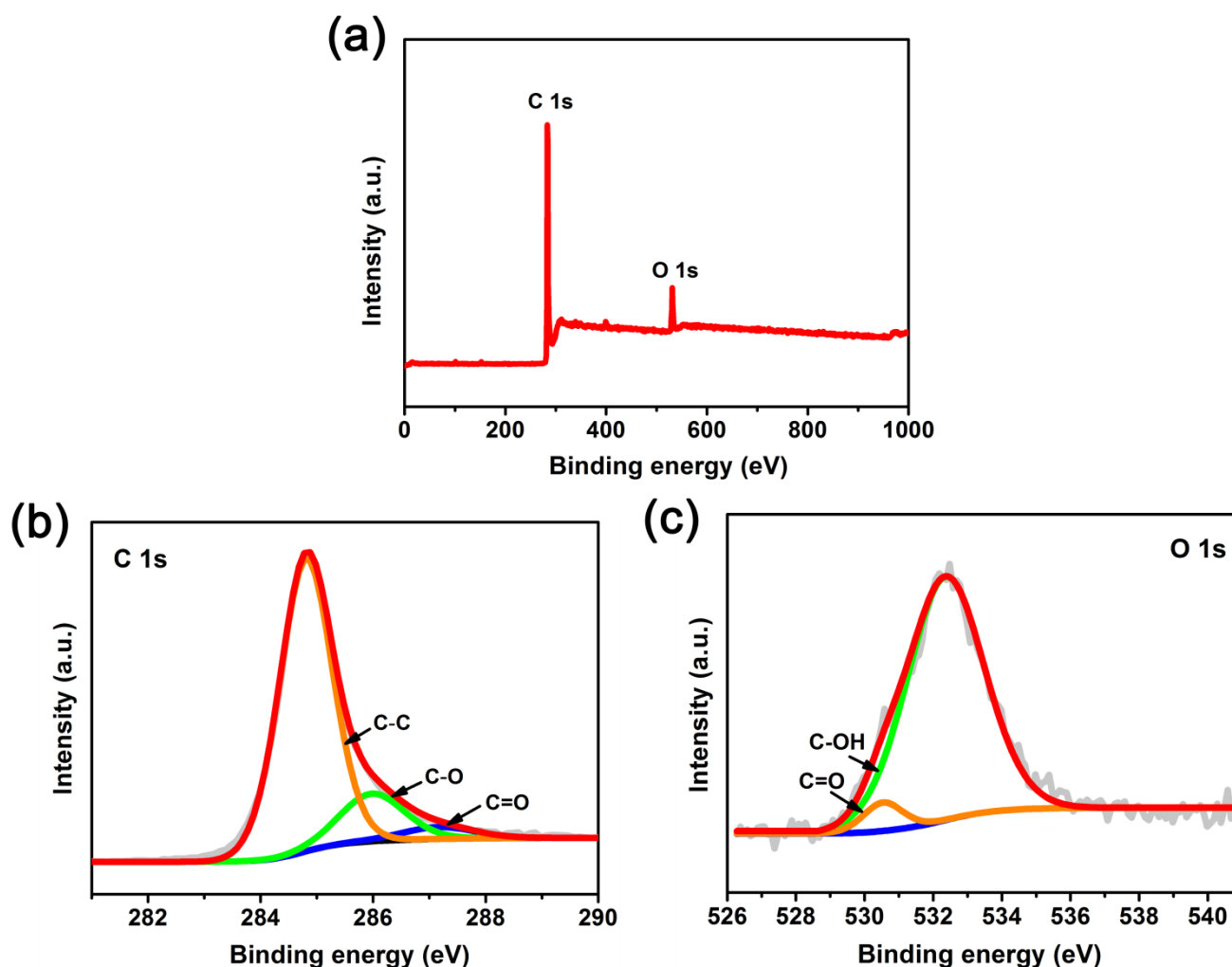


Figure 4. (a) XPS spectrum, (b) C 1s XPS spectra and (c) O 1s XPS spectra of the SCMs

XPS is applied to analyse the types of chemical elements and their chemical valences contained on the surface of the layer carbon materials. Figure 4 (a) presents the full XPS spectrum. The elemental peaks of carbon and oxygen can be clearly observed in the spectral region. It is indicated that the surface of the SCMs is mainly composed of the elements carbon and oxygen. After the carbon peak calibration, the C 1s and O 1s peaks are both subjected to peak fitting. The three peaks fitted to the C

1s signal in the XPS spectrum correspond to C-C bonds in the non-defective graphite lattice, as well as C-O bonds and C=O bonds in the defective graphite lattice. In the O 1s spectrum, there are two peaks corresponding to the C=O bond and the hydroxyl bond (C-OH). The oxygen-containing functional group can increase the reactive sites on the SCMs and improve the electrochemical reaction and Na⁺ storage capacity.

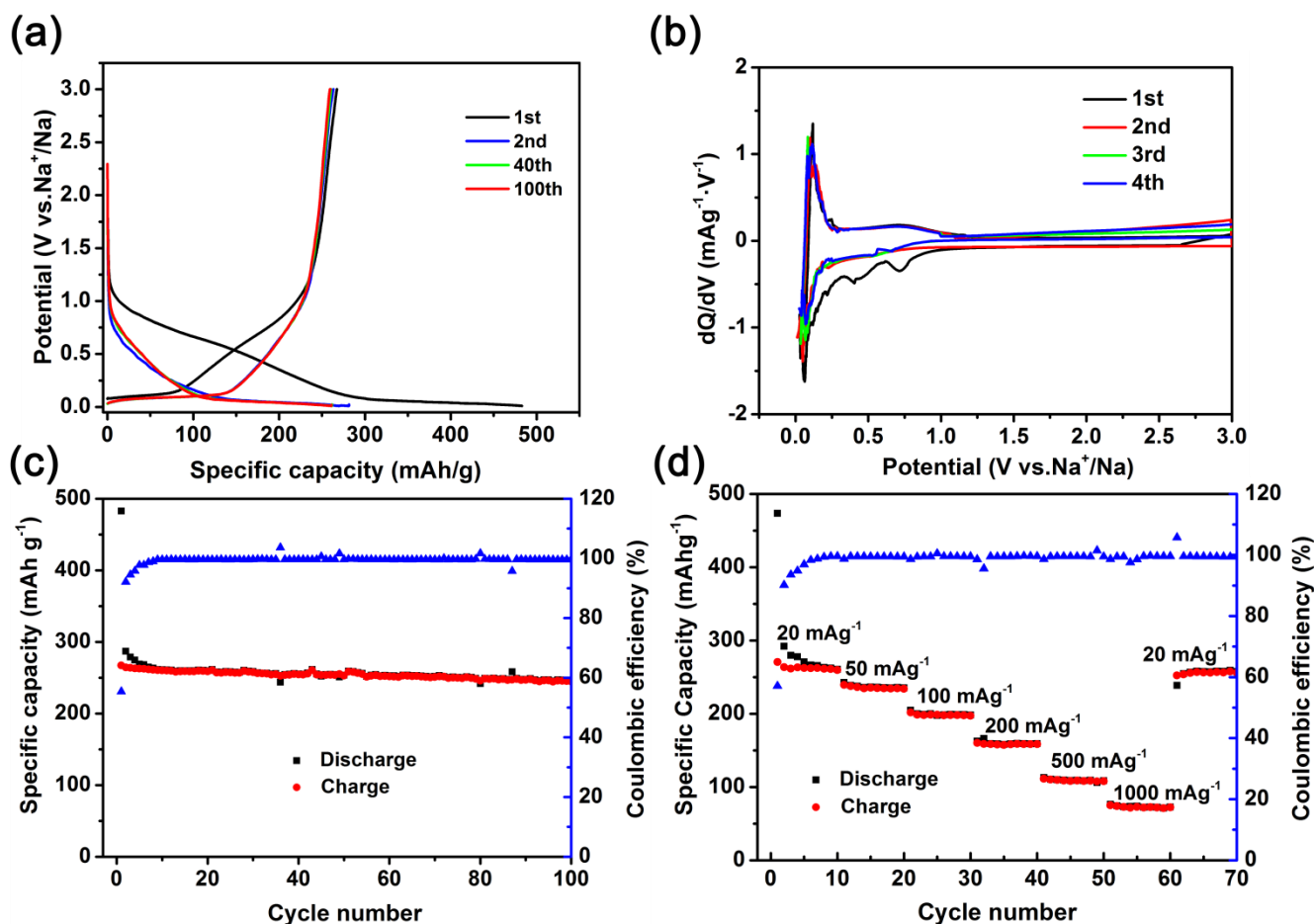


Figure 5. (a) Charge-discharge curves, (b) dQ/dV curve, (c) cycling performance and (d) rate performance of the SCMs.

Figure 5a shows the charge-discharge curve of the SCMs electrode after one hundred cycles at 20 mA/g. In general, the charge-discharge curves of biomass carbon-sodium negative electrode materials can be classified by different electrochemical reactions, including high-potential surface adsorption-desorption slope curves and low-potential sodium ion insertion-desorption platform curves. Moreover, observing the initial cycle, it is evident that the specific discharge capacity and specific charge capacity are 482.8 and 267.7 mAh/g, respectively. With the second cycle, the discharge capacity decreases, obviously due to the irreversible reaction. However, as the number of cycles increases, the battery exhibits excellent electrochemical cycling stability performance because a solid electrolyte interface (SEI) stably exists in an irreversible reaction.

As shown Figure 5b, the charge-discharge data of the SCMs are integrated to obtain dQ/dV to

analyse the charge-discharge voltage platform of the electrode. The figure shows the dQ/dV curve drawn by four cycles of PBC. In the initial cycle, small peaks of 0.4 and 0.7 V different from those of other periods can be found. However, as the number of cycles increases, the two reduction peaks disappear, which corresponds to the charge-discharge curve. It is seen from the figure that there is a reduction peak at 0.05 V and oxidation peak at 0.1 V, representing the characteristic redox peak of sodium-ion insertion and deintercalation in graphite crystallites. The low potential platform provides most of the capacity of the SCMs electrode. The good coincidence of the dQ/dV curves in the following three cycles shows that the SCMs has fine cycling reversibility for sodium-ion storage.

Figure 5 (c) displays the electrochemical cycle stability of the SCMs electrode at 20 mA/g. After 100 cycles, it still achieves a reversible capacity of 261.1 mAh/g with a coulombic efficiency of 99.4%. The lower coulomb efficiency in the initial cycle may be due to the formation of the SEI membrane and the occurrence of an irreversible reaction. The formed SEI film helps to improve the cycling stability of the SCMs electrode and maintain a high coulombic efficiency in subsequent cycles. The SCMs electrode material exhibits excellent rate performance, as shown in Figure 5 (d). At current densities of 20, 50, 100, 200, 500 and 1000 mA/g, the discharge capacity can reach 261.1, 235.4, 199.1, 159.3, 108.8 and 72.8 mAh/g, respectively. When the value is returned to 20 mA/g, the SCMs electrode can still reach a reversible capacity of 257.3 mAh/g, indicating that the SCMs can achieve a high cycle reversible capacity under high current charge and discharge.

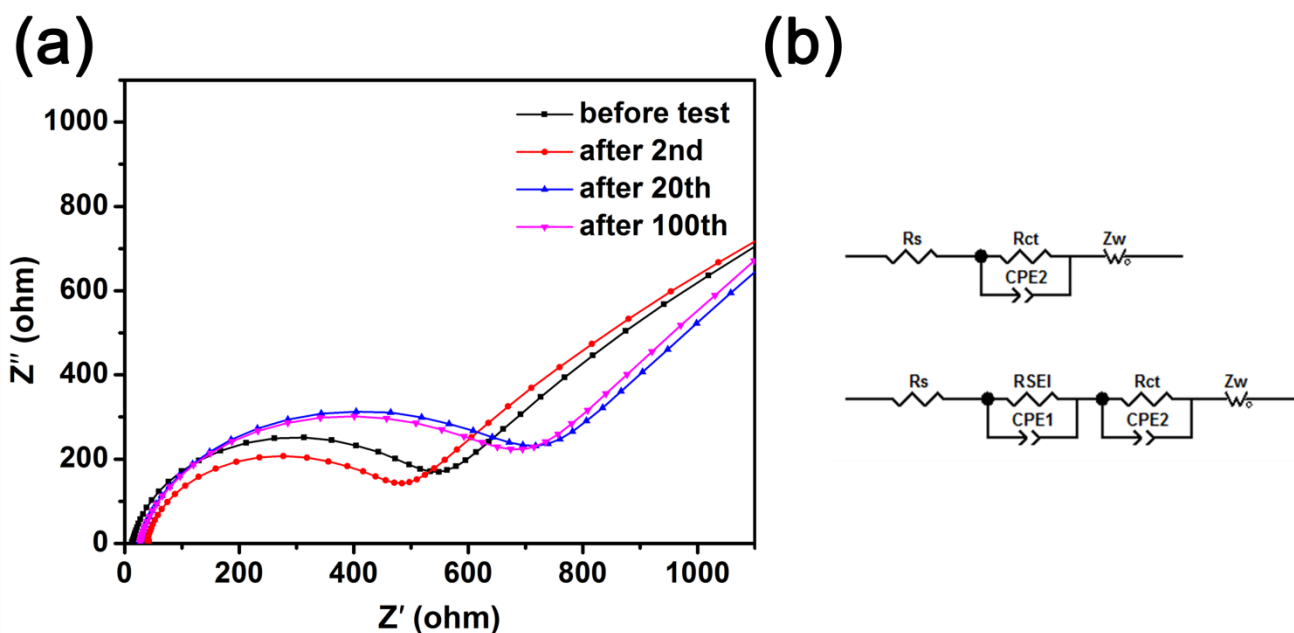


Figure 6. (a) The electrochemical impedance spectroscopy (EIS) results of the SCMs electrode before and after cycling. (b) The equivalent circuits.

Table 1. This work is compared with other biomass carbon anodes of SIBs

Biomass carbon	Cyclic stability	Reference
SCMs	261.1 mAh g ⁻¹ at 20 mA/g (100 cycles)	Present work
paulownia shells	179 mAh g ⁻¹ at 50 mA/g (100 cycles)	[27]
argan shells	300 mAh g ⁻¹ at 25 mA/g (70 cycles)	[28]
pistachio shells	225 mAh g ⁻¹ at 10 mA/g (100 cycles)	[29]
hemp stem	256 mAh g ⁻¹ at 0.1 C (100 cycles)	[30]
human hair	201 mAh g ⁻¹ at 100 mA/g (100 cycles)	[31]

As shown in Figure 6a, through performing the EIS test on the SCMs electrode for different cycle periods, the impedance change during the electrode cycle can be determined. In general, the electrochemical impedance spectra display a semicircle and diagonal line at high-medium frequency and low frequency. The semicircle in the high-frequency region of the Nyquist diagram is related to R_s . Generally, R_s corresponds to ohmic resistance, which is related to the electrode material, the resistance of the electrolyte itself, and its interface contact resistance. Arcs appear in the high-frequency region and are related to the formation of the SEI membrane during cycling. R_{SEI} corresponds to the resistance of sodium ions to diffusion or migration through the SEI film, CPE is considered to be an electric double-layer capacitor, and this reaction process can be fitted with a parallel circuit of R_{SEI} and CPE. The intermediate frequency region is considered to be related to the charge transfer process. R_{ct} is the electrochemical reaction resistance, and R_{ct}/CPE parallel circuits are generally used to simulate the reaction process. The low-frequency diagonal is attributed to the diffusion Warburg impedance (ZW). Figure 6b shows the equivalent fitting circuit. It is generally considered that the SEI membrane is generated during electrochemical cycling, so the R_{SEI} of the electrode before the cycle can be ignored. According to existing research, when the number of battery cycles increases, the electrolyte and the SCMs accelerate the loss, so the resistance during the charge transfer reaction increases, causing R_{ct} to increase. The results show that the formation of the SEI membrane on the SCMs electrode mainly occurs in the initial cycle and is accompanied by an increase in impedance. As the number of charges and discharges increases, the impedance gradually stabilizes.

Biomass carbon materials have received extensive attention in terms of sodium charged negative electrodes. Dou et al., used phosphoric acid to enhance the electrochemical performance of peanut shell carbon materials. Prolonged acid modification could increase the rate performance of the carbon material (122 mAh/g at 10 C) [23]. Guo's group used a template method to increase the number of holes in an the egg yolk material. The prepared carbon material showed a reversible capacity of 208 mAh/g, which after 200 cycles could maintain a high capacity of 86% [24]. Tekin's group used hydrothermal carbonization to prepare hard carbon derived from waste teabag powder, which was then physically activated. The HCMs has stable cycling characteristics, and a discharge capacity of 127 mAh/g at 100 mA/g [25]. In Tian's group, a porous kapok was made from phoenix tree leaf using a simple KOH activation method. The pore-forming agent makes the biomass carbon contain a large

number of micropores and a small amount of mesopores, thus having a high SSA. The porous carbon sample shows excellent cycle stability and rate performance. The specific capacity at 100 mA/g is 137 mA h/g, while the discharge capacity is 100 mAh/g at 1 A/g [26]. Table 1 lists the cyclic stability of biomass HCMs in recent years, it compares the performance differences of biomass carbon materials using different preparation methods. The present work has the advantages of high yield, a simple preparation process, environmental protection and excellent cycling performance.

Although the preparation process of biomass carbon materials described above in recent years is becoming increasingly complete, these processes are still far from those of industrial carbon materials. The use of pore-forming agents such as strong acids and bases is not conducive to environmental protection requirements, the template method has lower carbon yield and higher cost, and the hydrothermal method can increase the number of active sites on the surface of the material, but it is easy to produce wastewater. Therefore, laver with large SSA, high yield and low price was selected as the raw material in this experiment, which was calcined at 1200°C to form a hard carbon material with a lamellar structure. During the preparation process, there are no side reactions, and it has the characteristics of high carbon yield, low cost and environmental protection. The SCMs electrode has excellent cycle stability. After 100 cycles at 20 mA/g, the reversible capacity can reach 261.1 mAh/g, so it is a potential sodium negative electrode material.

4. CONCLUSION

In this paper, a laver-derived sheet-like hard carbon material prepared by high temperature carbonization at 1200°C. Through the characterization of macroscopic morphology and microstructure, it is observed that the SCMs carbon is a typical amorphous hard carbon material composed of disordered and disordered graphite microcrystals. Analysis of the BET results shows that the SCMs has a smaller SSA and more oxygen functional groups on its surface, which can increase the number of active surface sites. When it is assembled into an anode SIBs for testing, the SCMs exhibits a fantastic electrochemical performance, presenting an initial cycle capacity of 482.8 mAh/g and a initial coulombic efficiency of 55.37%. A capacity retention rate of 99.61% can be obtained after 100 cycles at a current density of 20 mA/g. Moreover, at a current density of 1000 mA/g, the reversible capacity of the electrode can still reach 73.8 mAh/g. The outstanding cyclic stability of these electrode materials may be due to the combined effects of the sheet-like morphology, small SSA, pore structure, and functional groups on the surface of the SCMs. These special properties facilitate the generation of a stable and uniform SEI membrane and promote the diffusion of sodium ions. At the same time, the number of defect sites of the material are increased, thereby partially improving and enhancing the storage of sodium ions.

ACKNOWLEDGEMENTS

We gratefully acknowledge the National Natural Science Foundation of China (Nos. 21965017 and 51764029) and the Provincial Natural Science Foundation of Yunnan (Nos. 2017FB085 and 2018FB087).

References

1. J. Y. Hwang, S. T. Myung and Y. K. Sun. *Chem. Soc. Rev.*, 12(2017)46.
2. H. S. Song, A. P. Tang, G. R. Xu, L. H. Liu, M. J. Yin, Y. J. Pan. *Int. J. Electrochem Sci*, 13(2018)5.
3. N. Yabuuchi, K. Kubota, M. Dahbi and S. Komaba. *Chem. Rev.*, 23(2014)114.
4. M. Sawicki and L.L. Shaw. *RSC Adv.*, 5(2015)65.
5. J. Górká, C. Vix-Guterl and C. Matei Ghimbeu. *J. Carbon Res.*, 2(2016)4.
6. N. Yabuuchi, K. Kubota, M. Dahbi, S. Komaba. *Chem. Rev.*, 114(2014)23
7. N. Sun, H. Liu and B. Xu. *J. Mater. Chem. A*, 3(2015)41.
8. D. Larcher and J. M. Tarascon. *Nat. Chem.*, 1(2015)7.
9. Z. Zhu, F. Liang, Z. Zhou, X. Zeng, D. Wang, P. Dong, J. Zhao, S. Sun, Y. Zhang and X. Li. *J. Mater. Chem. A*, 6(2018)4.
10. T. Yang, T. Qian, M. Wang, X. Shen, N. Xu, Z. Sun and C. Yan. *Adv. Mater.*, 28(2016)3.
11. C. Wang, J. Huang, H. Qi, L. Cao, Z. Xu, Y. Cheng, X. Zhao and J. Li. *J. Power Sources*, 358 (2017).
12. D. Qin and S. Chen. *J. Solid State Electrochem.*, 21(2017)5.
13. K. Kim, D. Lim, C. W. Han, S. Osswald, V. Ortalan and J. P. Youngblood. *ACS Sustainable Chem. Eng.*, 5(2017)10.
14. Y. Xiao, H. Chen, M. Zheng, H. Dong, B. Lei and Y. Liu. *Mater. Lett.*, 116 (2014).
15. W. Lv, F. Wen, J. Xiang, J. Zhao, L. Li, L. Wang, Z. Liu and Y. Tian. *Electrochim. Acta*, 176 (2015).
16. P. Liu, Y. Li, Y. Hu, H. Li, L. Chen and X. Huang. *J. Mater. Chem. A*, 4(2016)34.
17. X. X. Ren, S. D. Xu, S. B. Liu, L. Chen, D. Zhang, L. Qiu. *J. Electroanal. Chem*, 841(2019)
18. Z. S. Ma, H. Y. Zhang, Z. Z. Yang, Y. F. Zhang, B. Yu, Z. M. Liu. *J. Mater. Chem. A*, 2(2014)45
19. Y. Liu, J. S. Xue, T. Zheng and J. R. Dahn. *Carbon*, 34(1996)2.
20. S. Kurasawa, S. Iwamoto and M. Inoue. *Mol. Cryst. Liq. Cryst*, 387(2002)
21. D. S. Knight and W. B. White. *J. Mater. Res.*, 4(1989)2.
22. Y. Liu, L. Z. Fan and L. F. Jiao. *J. Mater. Chem. A*, 5(2016)4.
23. X. W. Dou, I. Hasa, D. Saurel, M. Jauregui, D. Buchholz; T. Rojo, S. Passerini. *ChemSusChem*, 11(2018)18
24. L. Guo, Y. An, H. Fei, X. Feng, L. Ci. *Mater. Technol*, 32(2017)10
25. B. Tekin, E. Demir, R. Demir-Cakan, *Mater. Technol*, 34(2019)9
26. Z. Q. Tian, S. J. Sun, X. Y. Zhao, M. Yang, C. H. Xu. *Funct Mater. Lett.*, 11(2018)6
27. P. Wang, X. J. Li, X. F. Li, H. Shan, D. J. Li, X. L. Sun. *J. Mater. Res*, 33(2018)9
28. M. Dahbi, M. Kiso, K. Kubota, T. Horiba, T. Chafik, K. Hida, T. Matsuyama, S. Komaba. *J. Mater. Chem. A*, 5(2017)20
29. K. Kim, D. G. Lim, C. W. Han, S. Osswald, V. Ortalan, J. P. Youngblood, V. G. Pol. *ACS Sustainable Chem. Eng.*, 5(2017)10
30. P. F. Wang, K. Zhu, Z. Y. Gong, R. Liu, K. Cheng, G. L. Wang, J. Yan, D. X. Cao, *J. Colloid Interface Sci*, 561(2020)
31. J. Ke. Ou, L. Yang and X. H. Xi. *J. Power Sources*, 24(2017)